Acta Biomaterialia 171 (2023) 519–531

Contents lists available at ScienceDirect

Acta Biomaterialia

journal homepage: www.elsevier.com/locate/actbio

Full length article

Amplification of oxidative damage using near-infrared II-mediated photothermal/thermocatalytic effects for periodontitis treatment

Xinyu Dai[a,c,1], Yiping Liu[a,b,1], Fanrong Meng[d], Qiqing Li[a], Fengxia Wu[a], Jianguo Yuan[a], Haoran Chen[a], Huixin Lv[a,b], Yanmin Zhou[b,*], Yulei Chang[a,*]

[a] State Key Laboratory of Luminescence and Applications, Changchun Institute of Optics, Fine Mechanics and Physics, Chinese Academy of Sciences, Changchun, Jilin 130033, PR China
[b] Department of Oral Implantology, School and Hospital of Stomatology, Jilin University, Changchun, Jilin 130021, PR China
[c] Department of Oral and Maxillofacial Surgery, School and Hospital of Stomatology, Jilin University, Changchun, Jilin 130021, PR China
[d] Department of Stomatology, Aviation General Hospital, Beijing 100000, PR China

ARTICLE INFO

Article history:
Received 17 April 2023
Revised 13 August 2023
Accepted 10 September 2023
Available online 13 September 2023

Keywords:
Photothermal therapy
Nitric oxide
Peroxidase-like activity
Biofilm eradication
Periodontitis
Synergistic effect

ABSTRACT

Periodontitis is a biofilm-related disease characterized by damage to the periodontal tissue and the development of systemic diseases. However, treatment of periodontitis remains unsatisfactory, especially with deep-tissue infections. This study describes rationally designed multifunctional photothermocatalytic agents for near-infrared-II light-mediated synergistic antibiofilm treatment, through modification of Lu-Bi_2Te_3 with Fe_3O_4 and poly(ethylene glycol)-b-poly(l-arginine) (PEG-*b*-PArg). Notably, 1064-nm laser irradiation led to photothermal/thermocatalytic effects, resulting in the synergistic generation of reactive oxygen species (ROS) and reactive nitrogen species (RNS) and consequent damage to the biofilm. This treatment was based on the thermoelectric and photothermal conversion properties of Lu-Bi_2Te_3, the peroxidase-like catalytic capacity of Fe_3O_4, and the guanidinium polymer, PEG-*b*-PArg. Oxidative damage to biofilm was further enhanced by H_2O_2, resulting in the effective elimination of biofilm both *in vitro* and *in vivo*. These findings suggest that this synergistic therapeutic strategy is effective for the clinical treatment of periodontitis.

Statement of significance

The current treatment for periodontitis involves time-consuming and labor-intensive clinical scaling of the teeth. The present study is the first to assess the efficacy of a photothermal catalyst for periodontitis treatment. This used near-infrared-II light at 1064 nm to induce oxidative damage in the biofilm, resulting in its degradation. The synergistic photothermal/thermoelectric effect produced deep tissue penetration and was well tolerated, and can kill the biofilm formed by periodontitis pathogens up to 5 orders of magnitude, effectively treating the biofilm-induced periodontitis.

1. Introduction

Biofilms are structurally complex bacterial communities, where the bacteria are encased in a self-produced extracellular polymeric matrix (EPS) [1,2]. Biofilm-associated diseases represent a major public health hazard [2] with periodontitis being the sixth most common biofilm-associated disease worldwide [3]. Periodontitis is characterized by periodontal pockets, reduced tooth attachment, and alveolar bone loss, eventually leading to tooth loss [4]. Clinical treatment of periodontitis involves removing the plaque biofilms by scaling, root planing, and the use of antibiotics [4]. However, these treatments remain unsatisfactory due to the limited access of non-surgical mechanical debridement to deep periodontal pockets and furcation areas [5], the low susceptibility of biofilm to traditional antibiotics [6], and the increasing antibiotic resistance of bacteria [7]. It is thus necessary to find an effective solution to this problem.

Photothermal therapy (PTT) uses photothermal agents (PTAs) to convert harvested light into localized heat energy. It is a popular choice for the eradication of free bacteria and biofilm through hyperthermia-induced cell membrane destruction and protein de-

* Corresponding authors.
E-mail addresses: zhouym@jlu.edu.cn (Y. Zhou), yuleichang@ciomp.ac.cn (Y. Chang).
[1] These authors contributed equally to this work.

https://doi.org/10.1016/j.actbio.2023.09.014
1742-7061/

naturation [8,9]. However, there are few reports of the use of PTT for periodontitis treatment because of the difficulty of removing the deep-located lesions of periodontitis through traditional visible and first near-infrared (NIR-I) light-triggered PTT alone. [10]. Notably, NIR-II light-triggered PTT is a more appropriate alternative to NIR-I as it has the capability of deeper tissue penetration [11], and relatively high tolerance (i.e., tissue maximum permission exposure (MPE) of 1 W/cm^2 for NIR-II of 1064 nm and 0.33 W/cm^2 for NIR-I of 800 nm) [12,13]. It thus has the potential to solve the problems of PTT treatment of periodontitis. Thus, exploiting appropriate PTAs activated in the NIR-II window may have significant potential.

One nanomaterial, a bismuth-based chalcogenide Bi_2Te_3 nanosheet, was recently developed as a promising PTA for PTT due to its strong NIR-II absorption and high photothermal conversion efficiency (PCE) [14]. However, the thermoelectric effect of these nanosheets at near room temperature has rarely been explored in antibacterial applications. Thermoelectric materials can induce electron-hole separation, generate a voltage by utilizing temperature differences, and serve as thermocatalysts for the generation of the superoxide anion ($\cdot O_2^-$) and related catalytic activity [15]. It is worth noting that $\cdot O_2^-$ and its reduced form H_2O_2 are the two major reactive oxygen species (ROS) [16] that exert antibacterial action by inducing oxidative stress to damage biomolecules [17,18]. However, $\cdot O_2^-$ and H_2O_2 are not effective for removing biofilm. Notably, among various ROS, the hydroxyl radical (·OH) is one of the most potent oxidizing agents [19] and can bind covalently to biomolecules causing damage to DNA, lipids, and proteins [20,21]. Peroxidase (POD)-like enzymes can catalyze hydrogen peroxide (H_2O_2) to produce ·OH. The resulting destruction of cell membranes could increase the sensitivity of bacterial cells to heat [22], and the heat generated from the PTT could subsequently enhance the quantity of ·OH generated by the catalytic reaction [23].

In addition,$\cdot O_2^-$ and H_2O_2 can play additional bactericidal roles in cascade reactions that generate other chemicals, such as nitric oxide (NO) and peroxynitrite($ONOO^-$). The reaction between $\cdot O_2^-$ and NO generates the toxic byproduct, ONOO−, a reactive nitrogen species (RNS), that exerts nitrosative stress on biomacromolecules, thus killing bacteria. Thus, NO was introduced into the current treatments. Unlike conventional antibiotics, NO has been widely applied as a gas therapy as it has broad-spectrum bactericidal activities against biofilms [24]. It is reported to promote wound healing by accelerating collagen deposition during the recovery of wounds [25]. Recently, local NO release has been shown to protect against and partially reverse endothelial dysfunction in periodontitis, thereby protecting the cardiovascular system in patients with periodontitis [26]. Since NO is extremely reactive, a donor such as L-arginine (L-Arg), S-nitrosothiols (RSNOs), or N-diazeniumdiolates (NONOates) is used when designing a NO delivery system [27–30]. However, the rapid systemic clearance of RSNOs and the toxic NONOate byproducts limit their *in vivo* applications. Due to the presence of guanidine, biocompatible L-Arg can generate NO and L-citrulline catalyzed by NO synthase, H_2O_2, and singlet oxygen($^1O_2$) [25,28,31–33]. In addition, these positively charged polar amino acids and their derivatives [25] could also bind to biofilm surfaces by electrostatic adsorption since the bacterial surfaces are negatively charged [34]. Therefore, synergy between the ideal NO donors and the PTT/ROS system can enhance the effectiveness of the anti-biofilm treatment. Considering the heat resistance of tissue and the MPE of NIR light, to fully demonstrate the potential, safety, and efficacy of this combined treatment strategy for periodontitis, the most direct and effective methods would be to further increase the thermoelectricity, improve the PCE, or synergize with other cascade methods to generate sufficient ROS/RNS.

In this study, a synergistic nanoplatform comprising PTT and heat-induced ROS/RNS was developed for eradicating biofilm and promoting the recovery of infected sites (Fig. 1). The procedure involved the decoration of POD-like Fe_3O_4 and PEG-*b*-PArg on Lutetium-doped Bi_2Te_3 nanoplates to form BFA NPs (PEG-*b*-PArg-modified Lu-Bi_2Te_3@Fe_3O_4). As the photothermocatalyst, Bi_2Te_3 mediated NIR-II-triggered PTT for direct bacterial killing. The thermoelectric performance of the Bi_2Te_3 was further improved by using the Lu dopant, which can simultaneously reduce the κ_{ph} by alloy-scattering and optimizing the carrier concentration [35,36], resulting in more $\cdot O_2^-$ and H_2O_2 production during the PTT course. Notably, H_2O_2 could react with Fe_3O_4 to generate highly toxic ·OH and catalyze PEG-*b*-PArg to produce NO. Further, $ONOO^-$ was generated once NO reacted with $\cdot O_2^-$. Additionally, positively charged PEG-*b*-PArg facilitated the adhesion of BFA NPs to the negatively charged bacterial surface [37]. The generated RNS and ROS can act as broad-spectrum antibacterial agents [38,39], primarily through damaging the cell membrane and DNA [40,41], increasing the sensitivity of the bacteria to heat. This study demonstrated that the synergistic PTT/ROS/RNS treatment was effective for biofilm-induced periodontitis and could potentially be developed to treat other bacterial infections.

2. Methods

2.1. Materials

Reagents, including α-pinene, triphosgene, diethyl ether, N, N-dimethylformamide (DMF), 1-Amidinopyrazole hydrochloride, triethylene glycol, polyvinylpyrrolidone (PVP), bismuth oxide (Bi_2O_3), tellurium dioxide (TeO_2), sodium hydroxide (NaOH), glycerol, iron acetylacetonate, Lu_2O_3, Tm_2O_3, Yb_2O_3, Er_2O_3, and 3,3′,5,5′-tetramethylbenzidine (TMB), were purchased from Aladdin (Shanghai, China). N-ε-benzyloxycarbonyl-L-lysine and HBr (5 mL, 33 wt.% in acetic acid) were obtained from Macklin (Shanghai, China). Hexane was bought from TIANTAI (Guangzhou, China). Tetrahydrofuran (THF) was provided by Innochem (Beijing, China). MPEG2000-NH_2 was purchased from Ponsure Biological (Shanghai, China).

2.2. Biofilm growth and harvesting

Five hundred microliters of bacterial solution (10^5 CFU/mL) were incubated in 48-well plates to form biofilms. *Escherichia coli* (*E. coli*, ATCC 25922) was cultured in lysogeny broth (LB), *Staphylococcus aureus* (*S. aureus*, ATCC 29213) was cultured in tryptic soy broth (TSB), and *Porphyromonas gingivalis* (*P. gingivalis*, ATCC 33277) and *Fusobacterium nucleatum* (*F. nucleatum,* ATCC 10953) were cultured in brain heart infusion (BHI) broth with 5 μg/mL hemin and 1 μg/mL menadione. *P. gingivalis* and *F. nucleatum* were cultured anaerobically. After the formation of the bacterial film, the medium was removed, the planktonic bacteria were carefully washed away with phosphate-buffered saline (PBS), and the biofilms on the 48-well plates were harvested.

2.3. Thermocatalytic antibacterial properties of Bi_2Te_3

To investigate the thermocatalytic antibacterial effects of Bi_2Te_3 NPs, planktonic bacteria and biofilms were both selected as models. After the addition of 100 μg/mL of material to the bacterial solutions (2×10^5 CFU/mL) or established biofilms, the test groups were subjected to three thermal cycles in a water bath. In each cycle, the wells were first exposed to a temperature of 45 °C in the water bath for 5 min, followed by incubation at 25 °C for 5 min. The plate counting method was used to measure the antibacterial properties.

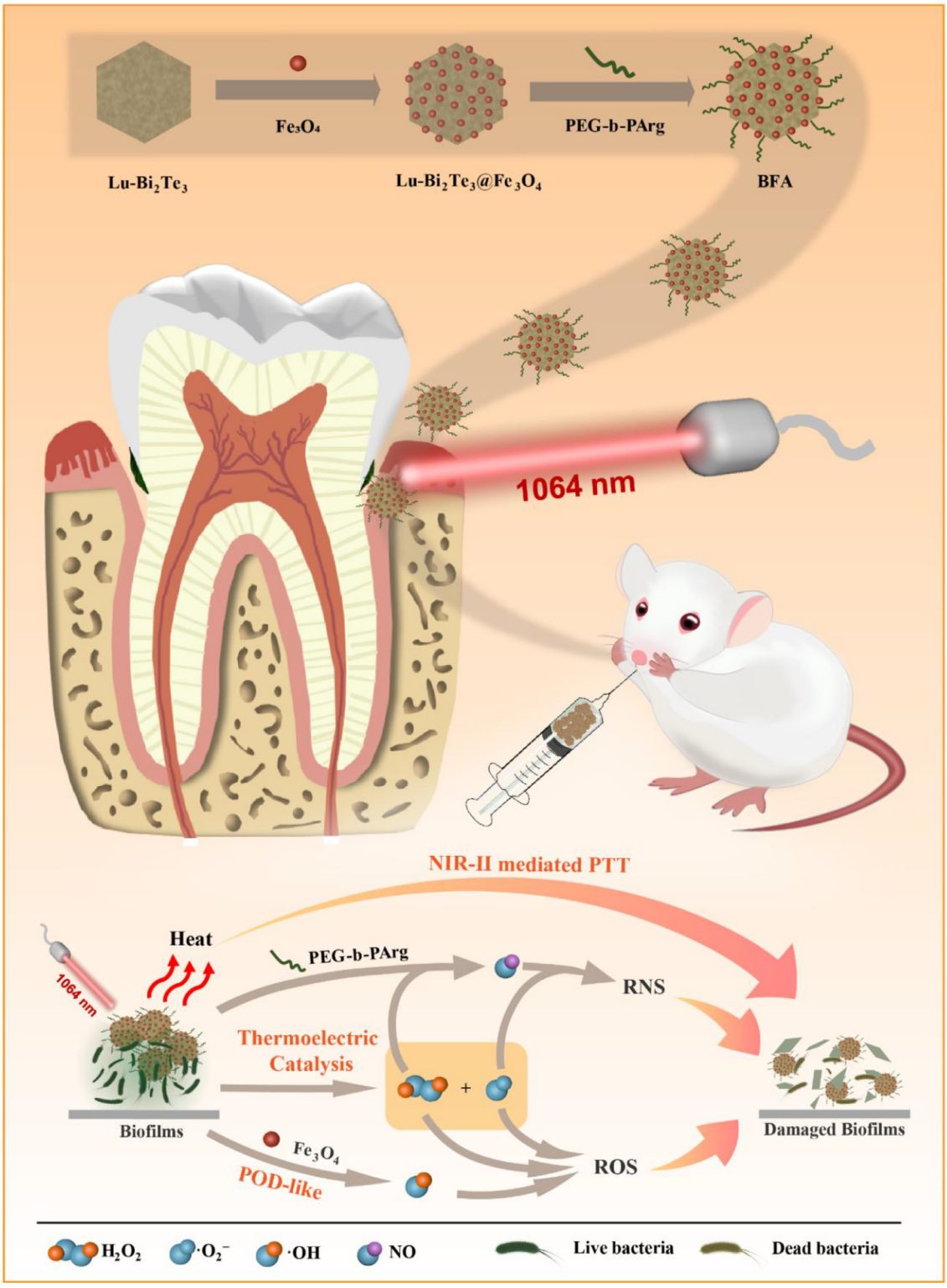

Fig. 1. Preparation and biomedical application of BFA. Lu-Bi_2Te_3@Fe_3O_4 was fabricated by a two-step solvothermal method. BFA was obtained by electrostatic attraction between Lu-Bi_2Te_3@Fe_3O_4 and PEG-*b*-PArg. A rat periodontitis model was used to evaluate the anti-biofilm activity of BFA, showing eradication of biofilms after treatment.

2.4. In vitro *antibiofilm activity evaluation*

The antibiofilm experiments were divided into twelve groups: (I) biofilms+PBS; (II) biofilms+H_2O_2; (III) biofilms+BFA; (IV) biofilms+BFA+H_2O_2; (V) biofilms+PBS+NIR-II; (VI) biofilms+H_2O_2+NIR-II; (VII) biofilms+BFA+NIR-II; (VIII) biofilms+BFA+H_2O_2+NIR-II; (IX) biofilms+BFL; (X) biofilms+BFL+H_2O_2; (XI) biofilms+BFL+NIR-II; (XII) biofilms+BFL+H_2O_2+NIR-II. The final concentrations of nanoplates and H_2O_2 in the wells of the plates were 100 μg/mL and 200 μM, respectively. After incubation for 1 h, groups V- VIII and XI-XII were subjected to three therapeutic cycles. In each cycle,

the wells were first exposed to NIR (1 W/cm^2) for 5 min, followed by incubation at 25 °C in a water bath for 5 min. After that, all groups were incubated at 37°C for another 3 h.

A standard plate counting assay was employed to assess the antibiofilm activity of BFA. The bacteria embedded in biofilms were dispersed in sterile PBS. After serial dilutions in PBS, 100 μL of *E .coli* and *S. aureus* suspensions were spread onto agar plates and incubated at 37 °C. After 24 h, the bacterial colonies were analyzed as follows:

$$\text{Antibiofilm ratio } (\%) = \frac{N_{control} - N_{experiment}}{N_{control}} \times 100\%$$

P. gingivalis and F. nucleatum were diluted according to the gradient point plate, and the difference in the dilution power was counted to calculate the bactericidal ability.

Scanning electron microscopy (SEM) was used to observe the morphology of biofilms. The treated biofilms were fixed with 2.5% (w/v) glutaraldehyde at 4°C for 4 h after being washed with PBS and dehydrated in gradient ethanol (30–100%). Finally, the samples were sprayed with gold for SEM observation.

SYTO 9 and propidium iodide (PI) stains (L13152 live/dead BacLight, Thermo Fisher Scientific) were employed to examine the live/dead state of bacteria in the biofilms. First, samples were stained with SYTO 9 (6 μM) and propidium iodide (30 μM) for 15 min in the dark at room temperature. Then, the stained biofilms were observed by a fluorescence microscope (Nikon, Japan).

2.5. Biocompatibility of BFA in vitro

Human gingival fibroblasts (HGFs) were incubated in Dulbecco's modified Eagle medium (DMEM) supplemented with 10% fetal bovine serum, 100 μg/mL streptomycin, and 100 U/mL penicillin. The cultures were maintained at 37 °C under 5% CO_2. MTT assays were used to measure the *in vitro* cytotoxicity of the BFA in HGFs. HGFs were seeded into 96-well plates (1×10^4 cells per well) overnight and then co-incubated with various concentrations of BFA ranging from 0 to 400 μg/mL for another 24 h. After that, the medium was removed, MTT solution (0.5 mg/mL, 100 μL) was added to each well, and then the mixture was cultured for 4 h. Finally, the solution was replaced with 200 μL of dimethyl sulfoxide. After the plates were shaken at room temperature for 15 min, the absorption value at 490 nm of each well was determined with a spectrophotometric microplate reader (Bio Tek ELX808, USA).

For morphological observation, HGFs (2×10^5 per well) were seeded in culture dishes overnight, and different concentrations of BFA were added and incubated for a further 24 h. After fixation with 4% paraformaldehyde, cells were stained with FITC-phalloidin (Solarbio, China) followed by DAPI (Beyotime, China) for 15 min each. The cells were then examined and imaged under confocal microscopy (Nikon, Japan). For analysis of the effects of BFA on cells, the cells were seeded and cultured as above, after which they were digested and washed twice with PBS. After staining with live-dead cell dye (Calcein/PI Cell Viability/Cytotoxicity Assay Kit, Beyotime, China) for 30 min, the cells were washed with PBS and analyzed by flow cytometry (FACSCalibur, Becton Dickinson, USA).

2.6. Rat experimental periodontitis model

All animal experiments complied with the protocols of the Jilin University Committee for Animal Use and Care. Twenty-five Wistar rats (male, 8 weeks old) were randomly assigned to five groups, namely, the (I) PBS, (II) H_2O_2, (III) BFA+H_2O_2, (IV) BFA+NIR-II, and (V) BFA+H_2O_2+NIR-II groups.

A model of experimental periodontitis was then established in all rats. Briefly, the bilateral maxillary first molars were ligatured by a 4-0 silk placed around the cervical region in the subgingival region for 7 days. These rats received sugar water (100 g/L) to accelerate microbial biofilm formation. Before treatment, the ligatures were all removed. Treatment for periodontitis was performed in the presence of BFA, H_2O_2, and NIR once daily for 7 days. In detail, BFA (100 μg/mL) and/or H_2O_2 (200 μM) were first injected locally into the gingival sulcus of the inflamed areas, after which the groups requiring irradiation were then exposed to 1064 nm laser (1 W/cm^2, 3 cycles of 5 min each). After treatment, all the animals were sacrificed, and the maxillae and major organs were harvested for further analysis.

Swabs of the plaque biofilms were collected from the molars for bacterial colony counting. First, the bacterial suspensions were serially diluted and then plated on the LB agar. After incubation for 24 h at 37 °C, the growing colonies were counted. Next, the hard tissues, including maxillae and teeth, were scanned by micro-CT (Bruker SkyScan, Antwerp, Belgium). For histological analysis, the maxillae were fixed and immersed in paraffin wax and then cut into tissue slices (5 μm thick). The sections were then stained with hematoxylin and eosin (H&E) or Masson's trichrome stain.

2.7. Characterization

Transmission electron microscopy (TEM, Tecnai F20, FEI, USA) was employed to obtain TEM, HRTEM, HAADF-STEM, and EDS element mapping images. The zeta potentials of different nanoplates were measured by a Malvern Zetasizer (NanoZS, Malvern, UK). XPS spectra were collected by X-ray photoelectron spectroscopy (Thermo ESCALAB 250Xi, Thermo Fisher Scientific, USA) for element analysis. X-ray diffraction (XRD, D8 FOCUS, Bruker, Germany) was employed to determine the crystalline structure.

2.8. Statistical analysis

All the experiments were performed at least three times. The data are presented as the means ± standard deviation, and different letters above the bars in the graphs indicate significant differences at $p < 0.05$. Differences were assessed by one-way ANOVA followed by Tukey's test for multiple comparisons.

3. Results and discussion

3.1. Synthesis and characterization of BFA

Fig. 1 illustrates the preparation of BFA NPs. First, the thermoelectric performance of rare-earth-doped Bi_2Te_3 was investigated, including Lu, Tm, Yb, and Er. A maximal amount of thermocatalytic generation of $\cdot O_2^-$ was obtained for Lu-Bi_2Te_3 consisting of 1% Lu (Fig. S1a, b). Notably, at a temperature difference of 20K, Lu- Bi_2Te_3 (100 μg/mL) could generate 13.68 μM $\cdot O_2^-$ and 1.2 μM H_2O_2 (Figs. S1a and 3f). Therefore, Lu-Bi_2Te_3 was selected and functionalized with Fe_3O_4 via a two-step solvothermal method. The proportions of the individual elements were measured by inductively coupled plasma mass spectrometry (ICP-MS), with the result Bi 24.7459%, Te 22.6642%, Fe 18.5817 %, and Lu 0.2340%, respectively. The crystalline structure of Lu-Bi_2Te_3@Fe_3O_4 was then determined by X-ray diffraction (XRD). The XRD patterns (Fig. S2) showed the co-existence of the diffraction peaks of Bi_2Te_3 at 27.7, 37.8, 41.1, 50.3, 57.1, and 62.3 and Fe_3O_4 at 30.1 (220), 35.4 (311), 43.1 (400), and 53.4 (422) as compared to the standard card of Bi_2Te_3 (JCPDS 15-0863) and Fe_3O_4 (JCPDS19-0629), confirming the successful preparation of Lu-Bi_2Te_3@Fe_3O_4 NPs. The as-obtained Lu-Bi_2Te_3@Fe_3O_4 was further functionalized with PEG-*b*-PArg polymer via electrostatic attraction. Specifically, the PEG-*b*-PArg block copolymer (Mn= ~9000 g/mol) was synthesized in three reaction steps: ring-forming, deprotection, and guanidation (Fig. S3). The

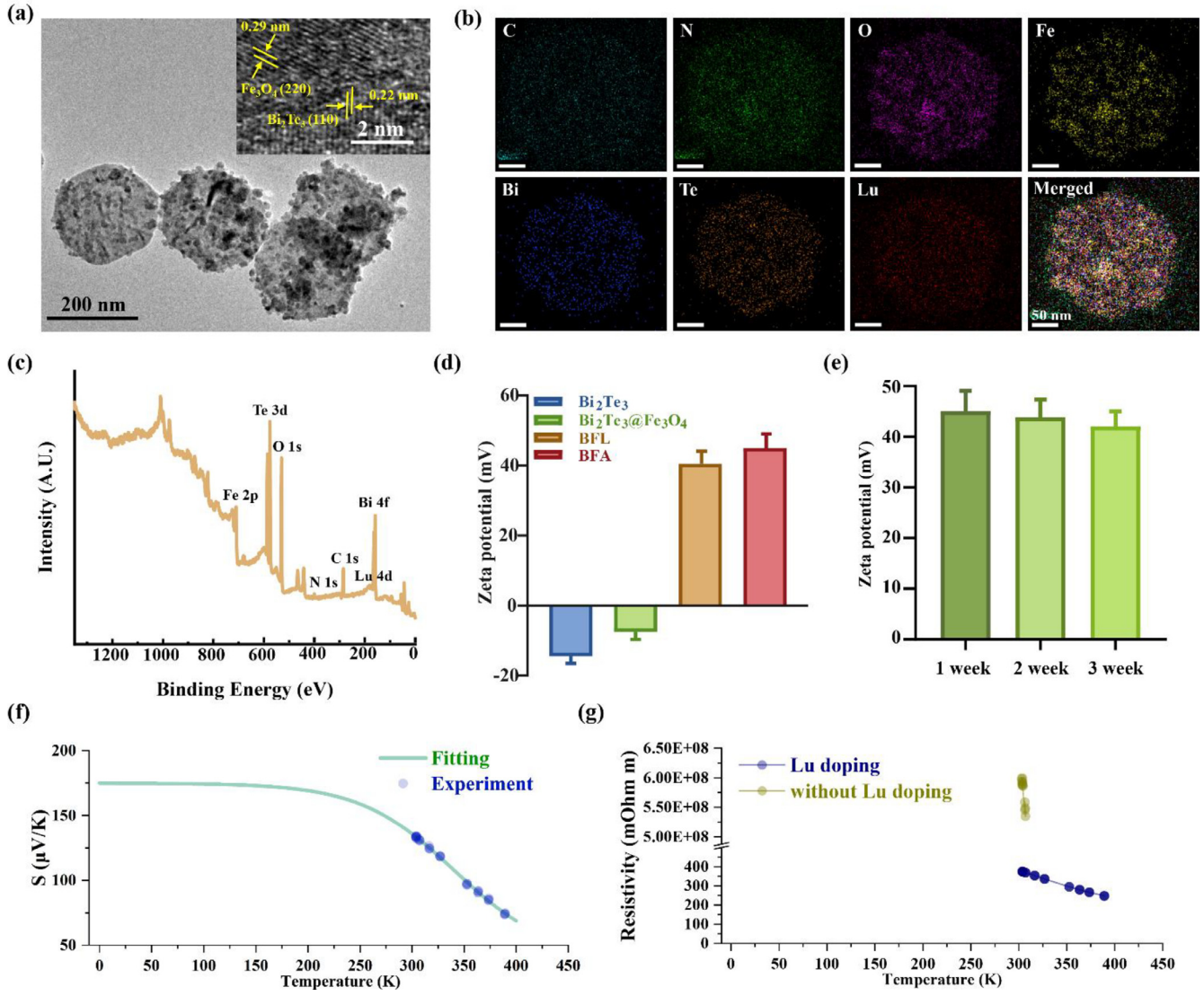

Fig. 2. Characterization of BFA. (a) TEM and HRTEM images of BFA. (b) Elemental mapping (C, N, O, Fe, Lu, Te, Bi) images of BFA. (c) XPS spectra of BFA. (d) ζ-Potentials of Lu-Bi_2Te_3, Lu-Bi_2Te_3@Fe_3O_4, BFL and BFA. (e) The zeta potential stability of the BFA nanoplates. (f) Measured and expanded Seebeck coefficient of Lu-Bi_2Te_3. (g) Temperature-dependent resistivity of Bi_2Te_3@Fe_3O_4 with or without Lu. Data represent mean ± SD (n = 3) and were analyzed by one-way ANOVA ($p < 0.001$) followed by Tukey's post-hoc test. Different letters above the bars indicate significant differences at $p < 0.05$.

analysis of the chemical shifts and integral area from the ^{1}H NMR spectra confirmed the successful synthesis of PEG-*b*-PArg (Fig. S4). The peak at δ 8.02 ppm was attributed to the HNCO-protons and δ 7.81ppm to the -NH_2 protons δ 1.18, 1.21. 1.3, 1.52, 2.74, and 3.47 ppm could be assigned to the protons of PArg. TEM images of the as-prepared BFA nanoplates (Fig. 2a, b) showed hexagonal nanoplates, 230 nm in diameter, with the deposition of granular materials on their surface, indicating that Fe_3O_4 NPs were successfully assembled with Lu-Bi_2Te_3. High-resolution TEM (HR-TEM) images further revealed periodically arranged lattice fringes with an interatomic spacing of 0.22 nm corresponding to the (110) planes of Lu-Bi_2Te_3 and 0.29 nm corresponding to the (220) planes of Fe_3O_4 (Fig. 2a). Further, the element mapping images revealed the homogeneous distribution of the C, N, O, Fe, Lu, Te, and Bi elements in the BFA (Fig. 2b). X-ray photoelectron spectroscopy (XPS) was used to analyze the BFA's elemental composition and surface valence states (Fig. 2c). The high-resolution Fe 2p spectrum (Fig. S5a) revealed characteristic peaks with binding energies of 710.4 eV and 714.8 eV that could be attributed to Fe (2p3/2), and peaks at 723.8 eV and 731.7 eV to Fe (2p1/2), consistent with the valent values of Fe in Fe_3O_4 [42,43]. Meanwhile, the peaks at 159.1 eV and 164.4 eV were due to Bi (4f7/2) and Bi (4f5/2), respectively (Fig. S5b) and the two strongest peaks at 576 eV and 586.3 eV corresponded to Te (3d5/2) and Te (3d3/2), respectively (Fig. S5c). Furthermore, the PEGylation of Lu-Bi_2Te_3@Fe_3O_4 was confirmed by changes in the zeta (ζ) potential. At first, Lu-Bi_2Te_3@Fe_3O_4 NPs showed a negative ζ potential (−7.47 ± 2.2 mV), which increased to 45 ± 4 mV after the chelation with PEG-*b*-PArg. The formation of BFL (PEG-b-PLys-modified Lu-Bi_2Te_3@Fe_3O_4) NPs was also similarly confirmed (40.5 ± 3.6mV), suggesting the positively charged guanidine or amine neutralized the negative charges of Lu-Bi_2Te_3@Fe_3O_4 (Fig. 2d). In addition, such large ζ potential values, long-term zeta potential stability (Fig. 2e), and long-term stability in physiological solution (Fig. S6) further reflected colloidal stability, which is critical for biological applications.

The thermoelectric properties of the samples were next investigated, as illustrated in Fig. 2f. Unsurprisingly, the Seebeck coefficient of the sample exhibited a typical negative temperature-dependent feature, indicating that the classic charge carrier dominant was not the same as that in the Ref. [44], where the

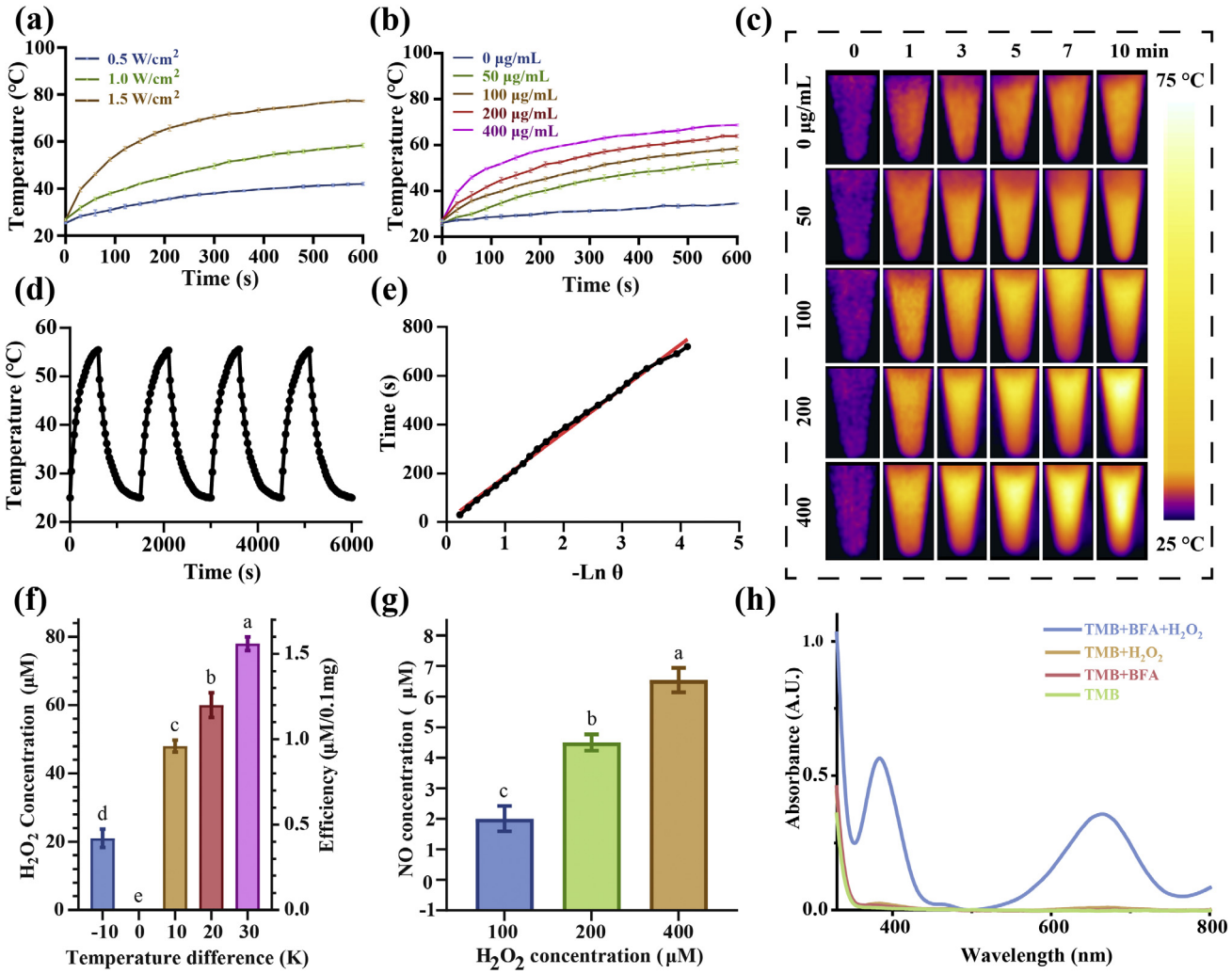

Fig. 3. Functional analysis of as-synthesized BFA. (a) Temperature changes of BFA (100 μg/mL) with different 1064 nm irradiation power (0.5, 1.0, 1.5 W/cm^2). (b) Temperature change curves of BFA at different concentrations (0, 50, 100, 200, 400 μg/mL) under NIR irradiation (1 W/cm^2). (c) Thermal images of BFA with different times and concentrations under 1064 nm irradiation (1 W/cm^2). (d) Photothermal stability test of BFA under irradiation with 4 on/off cycles. (e) Linear time data versus –ln θ was obtained from the cooling period. (f) Lu-Bi_2Te_3-mediated (5mg/mL) H_2O_2 generation under different temperature differences. (g) NO release from BFA (100 μg/mL) under H_2O_2 incubation (0, 100, 200, 400 μM). (h) UV-vis absorption spectra of TMB solution with different treatments (BFA: 100 μg/mL). Data represent mean ± SD(n = 3) and were analyzed by one-way ANOVA ($p < 0.001$) followed by Tukey's posthoc test. Different letters above the bars indicate significant differences at $p < 0.05$.

phonon scattering behaviors were more suited to describe the temperature-regulated Seebeck coefficient.

The Seebeck coefficient in metal systems can also be written as the Mott formula as follows:

$$S = \frac{\pi^2 k_B^2 T}{3e} \frac{\sigma'(\varepsilon_F)}{\sigma(\varepsilon_F)}$$

Where σ represents the energy-dependent electrical conductivity, the resistivity of the BFA sample at different temperatures was measured to verify the evolution pattern corresponding to the thermoelectric behaviors (Fig. 2g). On the one hand, it also showed obvious temperature-dependent characteristics. The measured sample resistivities indicated that the system used in this research was still semi-conductive. Thus, the intrinsic mechanism reflected from the Mott formula also revealed that the thermoelectric behavior of the sample was phonon-scattering controlled.

Interestingly, Lu doping significantly improved BFA's electrical conductivity. The reason may is that carrier tunneling appeared through heterogeneous interfaces among Fe_3O_4 NPs thus, their bulk electric conductivity increased. In addition, Lu-doped BFA showed thermoelectric performances as high as ~100 μV/K level. This phenomenon was also indicated in the subsequent *in vivo* applications.

3.2. Photothermal properties of BFA

The temperature of the BFA solutions (100 μg/mL) increased rapidly from 25 °C to 41.2 °C even at low power densities (0.5 W/cm^2), as shown in Fig. 3a–c. Additionally, the temperature of the BFA solutions at a low concentration (50 μg/mL) increased remarkably (ΔT=16.8 °C) compared with DI water (Δ=8 °C) after a 10-min exposure to 1064 nm light at 1 W/cm^2. The temperature of 400 μg/mL BFA solutions was increased to 74 °C (ΔT=49 °C) at 1 W/cm^2 irradiation, indicating photothermal conversion. The corresponding absorption spectra in the near-infrared II region are shown in Fig. S7. Next, the photothermal stability of BFA was determined by irradiation with 1064 nm light at 1 W/cm^2 for 4 ON/OFF cycles. As shown in Fig. 3d, the temperature elevation curve of the BFA solution did not show any significant change during the repeated irradiation, revealing their photothermal stability. The PCE (η) of BFA was calculated to be 34.14 % in DI water (Fig. 3e). Thus, put together, these results confirm that BFA could be an ideal PTA for NIR-II PTT.

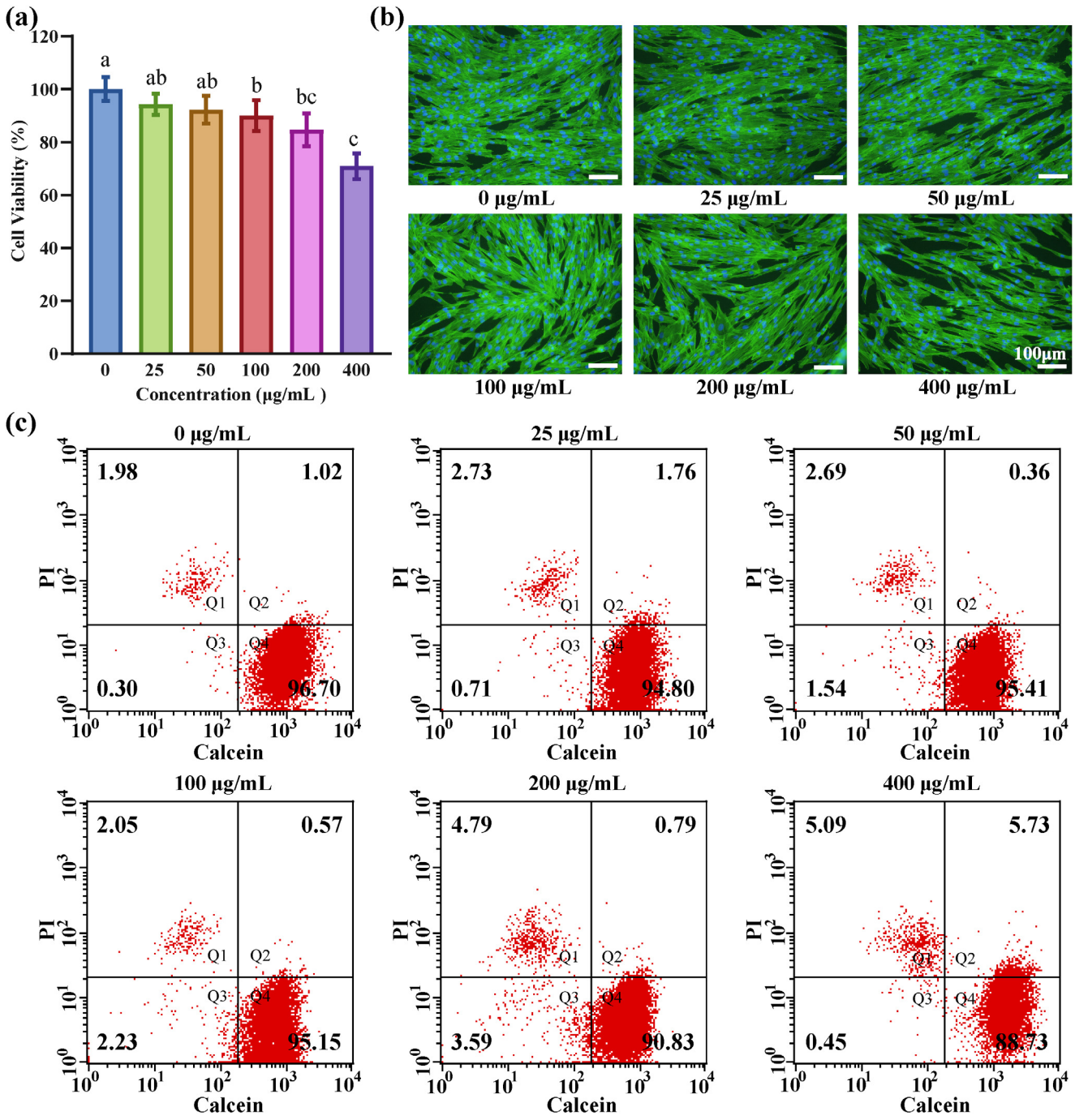

Fig. 4. Biosafety assay of BFA. (a) Proliferation of HGFs incubated with different concentrations of BFA (0, 25, 50, 100, 200, 400 μg/mL) for 24 h. (b) Fluorescent images of staining in HGFs after incubation with various concentrations of BFA for 24 h. (c) Flow cytometry was used to detect the proportion of live/dead cells with different concentrations of BFA in 24 h (Q4-live cell %). Data represent mean ± SD (n = 3) and were analyzed by one-way ANOVA ($p < 0.001$) followed by Tukey's posthoc test. Different letters above the bars indicate significant differences at $p < 0.05$.

3.3. *Detection of released ·OH and NO gas release* in vitro

NO release via ROS catalysis of guanidine was confirmed by the Griess assay. The detection principle is based on the fact that NO is readily oxidized to NO_2^- in aqueous solution, which reacts with the Griess reagent to generate colored compounds. The absorbance was recorded at 546 nm, and the content of NO could be calculated from the standard curve. As shown in Fig. 3g, the BFA-mediated NO production was H_2O_2 concentration-dependent within 100-400 μM. There was no NO production without H_2O_2 addition, and after being treated with 200 μM of H_2O_2, 4.5 μM NO was detected. Previous reports have shown that only 4 μM NO could effectively eradicate biofilms [25].

Moreover, TMB was employed to detect the generation of ·OH through POD-like reactions, as it can be oxidized into blue-colored TMB (oxTMB) by ·OH with an absorbance maximum at 652 nm. As shown in Fig. 3h, the solutions showed the strongest absorption peak at 652 nm in the presence of H_2O_2 (10 mM) and TMB (1 mM), indicating that the ·OH generation was triggered as Fe^{2+} was oxidized by H_2O_2. Furthermore, the catalytic activity was proportional to the BFA in the concentration range of 25-400 μg/mL (Fig. S8a). Since elevated temperatures can enhance POD-like cat-

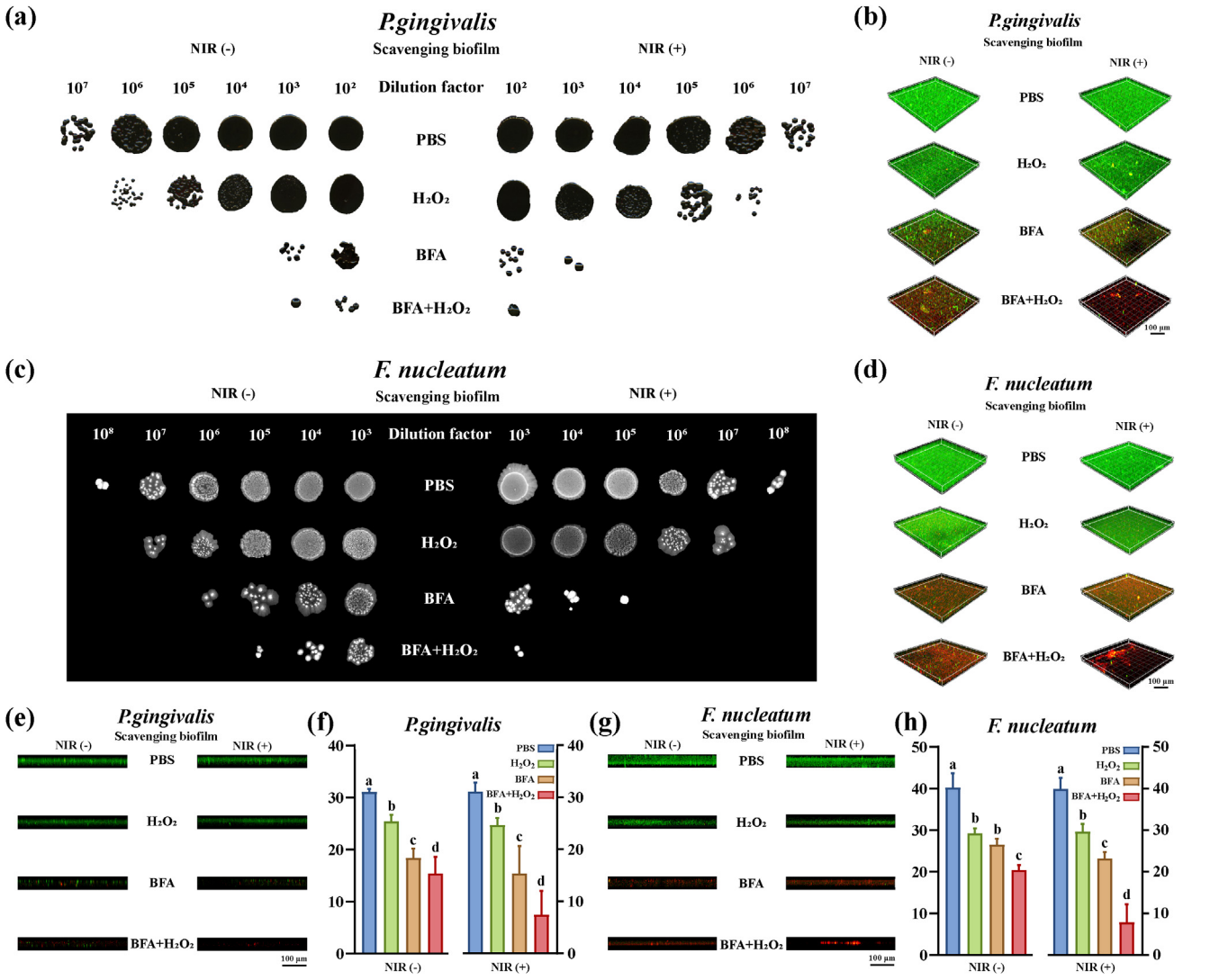

Fig. 5. Antibiofilm activity of BFA (100 μg/mL). (a,c) Images of bacterial colony formation after different treatments. (b,d) Live/dead 3D fluorescence staining images of biofilms after different treatments. (e,g) Fluorescence images of biofilm thickness. (f,h) The average thicknesses of biofilms in the different treatment groups were analyzed by one-way ANOVA ($p < 0.001$) followed by Tukey's post-hoc test. Different letters above the bars indicate significant differences at $p < 0.05$.

alytic capacity [22], the influence of temperature on the POD-like performance of BFA was investigated. As shown in Fig. S8b and c, the absorption intensity at 652 nm increased by 31.9% from 25-55 °C, indicating that the catalytic activity increased by 31.9%. Therefore, the enhanced reaction efficiency was attributed to the increased ionization with an increase in temperature [23]. Terephthalic acid (TA) was further employed to verify the generation of ·OH, based on TA could react with ·OH to produce fluorescent 2-hydroxyl terephthalic acid (TAOH) with an emission maximum at 435nm. As shown in Fig. S9, the obvious fluorescence peak confirmed the generation of ·OH.

3.4. In vitro *biocompatibility*

In addition to the physicochemical properties, biocompatibility is also essential for the bioapplications of BFA NPS. Thus, the *in vitro* cytotoxicity of different concentrations of BFA for human gingival fibroblasts (HGFs) was evaluated by MTT assays and Live/Dead cell staining, followed by flow cytometry. As shown in Fig. 4a, c, there was no obvious cytotoxicity after 24 h at BFA concentrations up to 100 μg/mL, while specific cytotoxicity was observed at 200 and 400 μg/mL, most likely due to ·OH generated by the POD-like catalysis. However, there were no noticeable changes in the cell morphology even at the high concentration of 400 μg/mL (Fig. 4b). In addition, the long-term toxicity of BFA, and the toxicities under various treatment conditions, are discussed in Supporting Information Fig. 10. These results indicate that BFA showed good biocompatibility *in vitro* and was consequently suitable for *in vivo* experiments.

3.5. In vitro *antibiofilm activity*

Encouraged by the positive effects of the BFA NPs, we investigated their synergistic anti-biofilm activity *in vitro* against the pathogenic periodontal bacteria, *P. gingivalis* and *F. nucleatum* (anaerobes), as well as the infection model bacteria *S. aureus* and *E. coli* (aerobic or facultative anaerobes, hereafter referred to as aerobes).

The plate counting method was first used to test the antibiofilm efficiency of the BFA NPs (Fig. S11). Lu-Bi_2Te_3 NPs alone were employed to exclude the effects of Fe_3O_4 and guanidium and reveal the thermoelectric catalytic abilities of BFA for antibacterial and biofilm removal. Notably, for planktonic bacteria, 75% *S. aureus* and 32.5% *E. coli* were killed under a temperature difference of 20 K

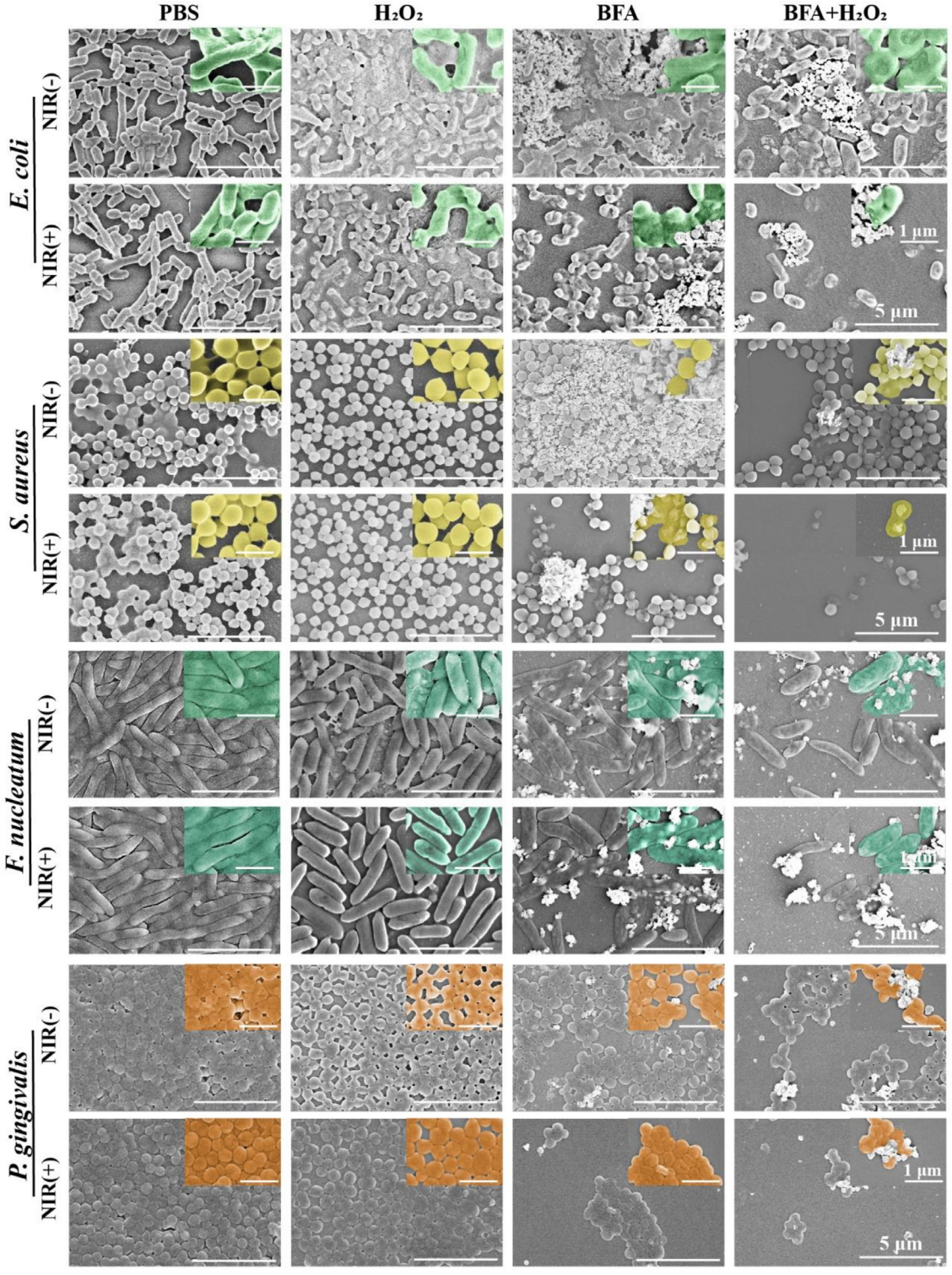

Fig. 6. Morphological analysis of biofilms (BFA: 100 μg/mL). SEM images of the morphological changes of biofilms after various treatments.

below 45°C in 3 thermal cycles (Fig. S12a), indicating that thermoelectric catalysis of Lu-Bi_2Te_3 could induce sufficient ROS to kill planktonic bacteria. However, only low antibiofilm efficiency could be observed under the same conditions (Fig. S12b), suggesting that a larger temperature difference or more prolonged treatment time was needed to generate sufficient ROS to eliminate biofilms. Incidentally, 3% H_2O_2 is commonly used in the clinical rinsing of periodontal pockets, and the residual H_2O_2 can be used for supplementary treatment after rinsing. Thus, a low concentration of H_2O_2 can trigger the related reaction of BFA or BFL. When biofilms were incubated with BFL and H_2O_2, the antibiofilm efficacies were 15% and 12% for *S. aureus* and *E. coli*, respectively, suggesting that the toxic ·OH generated by the POD-like reaction exhibited a limited antibiofilm effect (Fig. S13a, b). In contrast, the inhibition rates of biofilms treated with BFA and H_2O_2 were 31.25% and 25% for *S. aureus* and *E. coli*, respectively, indicating that the generated NO

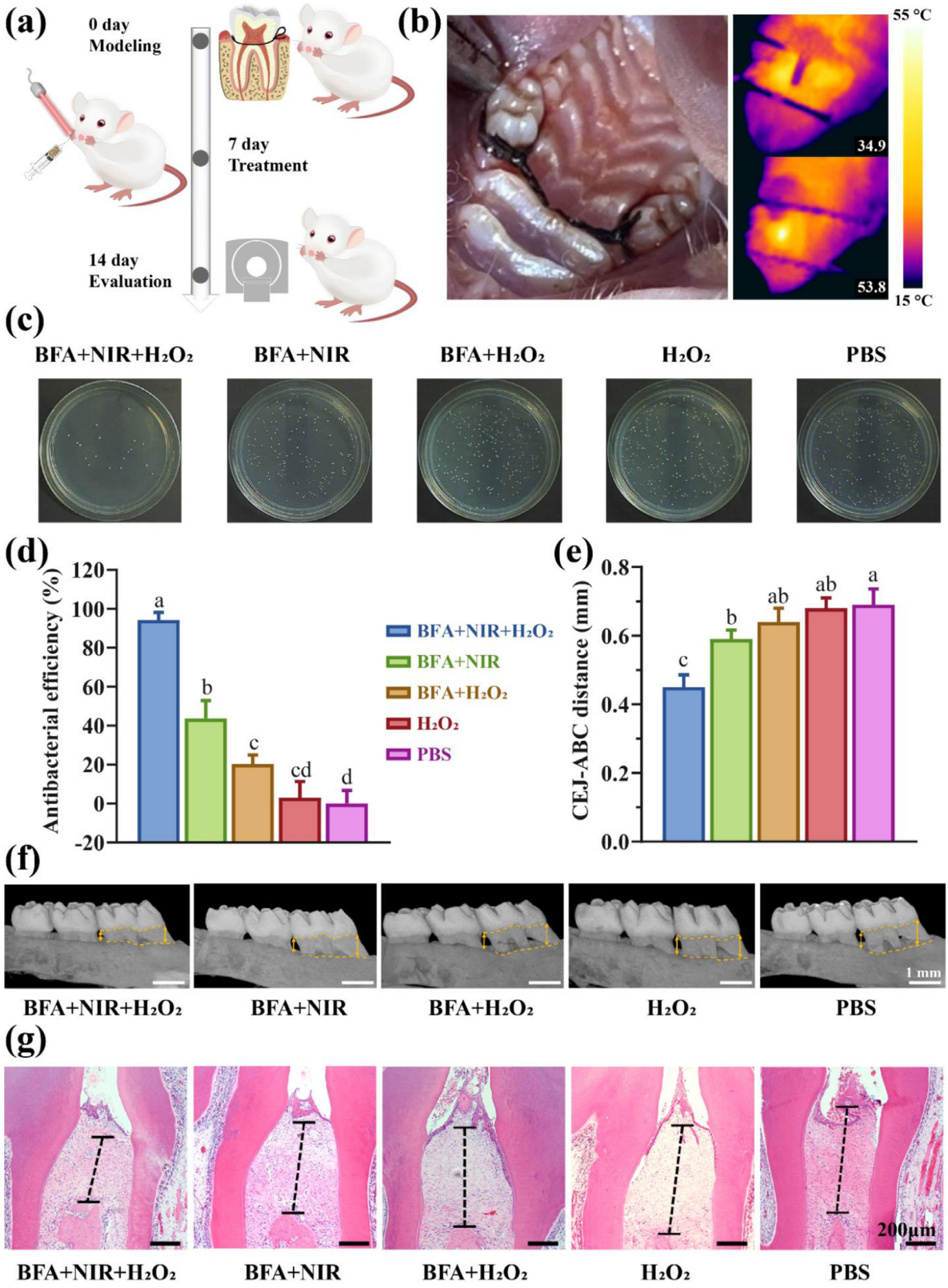

Fig. 7. *In vivo* anti-biofilm effects of BFA (100 μg/mL). (a) Schematic diagram of the process of periodontitis treatment. (b) *In vivo* real-time thermographic images under NIR irradiation (1064 nm, 1W/cm^2). (c, d) Bacterial colonies separated from the infectious sites on agar plates and corresponding quantitative analysis of antibacterial efficiency. (e) Corresponding quantitative analysis of CEJ-ABC distance. (f) 3D reconstructions of the maxillary molar area by micro-CT. The yellow dotted lines mark the distance between CEJ and ABC, and the double arrows indicate the ABL in the mesiobuccal and distobuccal regions. (g) Images of H&E-stained periodontal tissues from different treatment groups. Data represent mean ± SD($n = 3$) and were analyzed by one-way ANOVA ($p < 0.001$) followed by Tukey's post-hoc test. Different letters above the bars indicate significant differences at $p < 0.05$.

enhanced the treatment effects (Fig. S11b, c) due to the generated NO and ROS. The antibiofilm efficacies were 58.3% and 53% for *S. aureus* and *E. coli*, respectively, in the PTT/ROS synergistic treatment group (Fig. S11b, c). After treatment of the biofilms with BFL+H_2O_2+NIR-II, the antibiofilm efficacies reached 80% and 72% for *S. aureus* and *E. coli,* respectively (Fig. S13a, b). These enhanced antibiofilm properties may be related to the POD-like reaction induced by the addition of exogenous H_2O_2. The synergetic effect can be attributed to the heat produced in the PTT process that accelerated ·OH generation [45] and, consequently, ROS-mediated oxidative damage, enhancing the sensitivity of bacterial cells to heat [46]. Notably, when the biofilms were incubated with BFA+H_2O_2 and exposed to the 1064 nm laser, the antibiofilm efficacies were 97.5% and 92.5% for *S. aureus* and *E. coli,* respectively (Fig. S11b, c), demonstrating the enhanced antibiofilm activity of the PTT/ROS system in the presence of NO, indicating greater diffusion of NO into the interior of the biofilm [47]. In contrast, local hyperthermia only kills the bacteria on the biofilm surface [25]. Further, NO could also combine with $\cdot O_2^-$ to produce the highly toxic peroxynitrite (ONOO−). Notably, *S. aureus* was more sensitive to antibiofilm treatments than *E. coli,* mainly because the former contained more negatively charged surfaces that made interaction with the positively charged surfaces of BFA NPs more feasible. Moreover, although the cell walls of *E. coli* are thinner [48], *E. coli* grow much faster than *S. aureus* [49].

We then we used the gradient dilution method to explore the killing of anaerobic bacteria. In contrast to the aerobic bacteria, the anti-membrane effects were greatly improved in the anaerobic bacteria. It can be seen from Fig. 5a,c that the presence of exogenous hydrogen peroxide (200 μM) reduced nearly 1 log CFU, and the reduction was rapidly compensated for by the logarithmic growth of the remaining bacteria. BFA killed almost 2-3 log CFU of bacteria by thermoelectrocatalysis only. Interestingly, the synergistic effect of BFA+H_2O_2 and BFA+NIR resulted in essentially the same reduction in the numbers of *F. nucleatum,* reaching 3 log CFU, and *P. gingivalis,* reaching 4 log CFU. Under the combined action of the three agents, the bacterial biofilm was reduced by five orders of magnitude, indicating their coordination and joint action to achieve the best anti-membrane effect.

Scanning electron microscopy (SEM) was used to examine microstructural alterations in the biofilms after the different treatments. As seen in Fig. 6, there were numerous bacteria embedded in the extracellular polymeric substance (EPS), maintaining interconnections between the cells in the control group. EPS is composed mainly of proteins, extracellular DNA (eDNA), lipids, and polysaccharides, providing a stable 3-D structure for the biofilm to protect bacterial cells from the external environment and provide nutrition [50]. The bacteria also showed typical rod-shaped or spherical morphologies with integrated cell membrane structures. Surprisingly, numerous nanoplates were observed adhering to the biofilms due to electrostatic interactions. After H_2O_2 treatment, some cell walls appeared deformed, although most bacteria still clumped together, indicating that H_2O_2 could only cause limited damage to the bacteria. Both BFA+NIR-II and BFA+H_2O_2 killed more bacteria than the H_2O_2 group. The bacteria appeared collapsed, swollen, shriveled, or even cracked due to cell lysis [51]. Notably, the most severe damage to the bacteria was caused by treatment with BFA+H_2O_2+NIR-II, implying that PTT assisted by ROS and RNS resulted in significant antibiofilm activity.

Live/dead (green/red) staining assays were done to evaluate the synergistic antibiofilm effects. Green fluorescence-labeled STYO-9 indicated live bacteria, and red fluorescence-labeled PI indicated dead bacteria. Samples treated with BFA+NIR-II and BFA+H_2O_2 displayed relatively strong red fluorescent signals and relatively weak green fluorescent signals compared with those treated with PBS, H_2O_2, NIR-II, H_2O_2+NIR-II, and BFA, indicative of biofilm degradation resulting from hyperthermia or ROS. Further, almost all biofilms emitted red fluorescence after treatment with BFA+H_2O_2+NIR-II, indicating that the cell membranes were severely damaged (Fig. 5b,d). In addition, the vast majority of bacterial biofilms were completely removed. After combined treatment, the antibiofilm effect was evaluated by the biofilm thickness (Fig. 5e,g). The thickness of *P. gingivalis* biofilm was significantly reduced from 31.09 ± 1.58 μm to 7.40 ± 4.26 μm, while that of *F. nuucleatum* was reduced from 39.89 ± 2.48 μm to 7.85 ± 4.02 μm (Fig. 5f,h). This result also reflected significant biofilm removal.

3.6. In vivo *antibiofilm performance of BFA*

A model of experimental periodontitis was established in rats to explore the antibiofilm activity of BFA *in vivo*. The details of the establishment and treatment of animal periodontitis models are shown in the schematic diagram in Fig. 7a. The ∞-ligature method (Fig. 7b) was used on the first maxillary molars of the rats. The infected rats were randomly divided into five groups with different treatments (PBS, H_2O_2, BFA+H_2O_2, BFA+NIR-II, and BFA+H_2O_2+NIR-II). First, the *in vivo* photothermal performance of BFA-treated samples was evaluated (Fig. 7b). After NIR-II irradiation (1 W/cm^2, 5 min), the temperature of the region affected by periodontitis increased from 34.9 °C to 53.8 °C, demonstrating the ability of BFA to produce photothermal effects *in vivo*. After 7 days of treatment, the bacteria around the infected site were cultured and counted after spreading on plates for a quantitative evaluation of the antibiofilm activity after seven days of treatment. The antibacterial efficacy of BFA+H_2O_2+NIR-II reached 94.3 %, indicating its ability to destroy biofilm (Fig. 7c, d). Further, micro-CT analysis was used to determine the alveolar bone loss (ABL) due to inflammation (Fig. 7f). The degree of ABL is defined as the distance between the cementoenamel junction (CEJ) and the alveolar bone crest (ABC), taking the average of the mesiobuccal and distobuccal distances. Notably, BFA+H_2O_2+NIR-II treatment decreased the linear CEJ-ABC distance compared to PBS, H_2O_2, BFA+H_2O_2, and BFA+NIR-II (Fig. 7e). Thus, the results verified that BFA-mediated synergistic therapy efficiently eradicated biofilms, inhibited inflammatory bone resorption, and promoted soft tissue repair. In addition, the *in vivo* biosafety was further evaluated by histological images of the stomach after gavage and H&E staining of the major organs, including the heart, lung, liver, spleen, and kidney (Figs. S14,15). The results revealed no damage or histological abnormalities. Based on these results, it can be concluded that BFA NPs hold great potential in the clinical therapy of biofilm-induced periodontitis.

4. Conclusion

In summary, a PTT and heat-mediated ROS and RNS synergistic system was established for the treatment of biofilm-induced periodontitis based on the photothermocatalytic activity of BFA NPs. The positive charges on the BFA NPs facilitated binding to the negatively charged bacterial surfaces. Further, the thermoelectric and photothermal effects of the NPs led to the simultaneous generation of PTT and ROS under 1064 nm irradiation. The generated ROS then reacted with Fe_3O_4 and PEG-*b*-PArg to generate ·OH and NO, leading to the effective eradication of the biofilm by the generated heat, ROS, and RNS both *in vitro* and *in vivo*. Further, the results of the study demonstrated that the released NO could also promote tissue healing by stimulating angiogenesis and alleviating the damage caused by periodontitis. Thus, this nanoplatform provides an advanced strategy for the treatment of periodontitis in the clinic as well as other biofilm-induced deep-tissue infections.

Declaration of Competing Interest

The authors declare that they have no known competing financial interests or personal relationships that could have appeared to influence the work reported in this paper.

Acknowledgments

We gratefully acknowledge the financial support provided by the National Natural Science Foundation of China (62075217, 11874354, 11874355, 61575194 and 82071152), Project of Science and Technology Agency, Jilin Province (20210101148JC, 20230508104RC and 202512JC010475440), and the State Key Laboratory of Luminescence and Applications (SKLA-2019-02, SKLA-2020-09).

Supplementary materials

Supplementary material associated with this article can be found, in the online version, at doi:10.1016/j.actbio.2023.09.014.

References

[1] S. Fulaz, S. Vitale, L. Quinn, E. Casey, Nanoparticle-biofilm interactions: the role of the EPS matrix, Trends Microbiol. 27 (11) (2019) 915–926.
[2] J.L. Del Pozo, Biofilm-related disease, Expert Rev. Anti Infect. Ther. 16 (1) (2018) 51–65.
[3] M.A. Peres, L.M.D. Macpherson, R.J. Weyant, B. Daly, R. Venturelli, M.R. Mathur, S. Listl, R.K. Celeste, C.C. Guarnizo-Herreño, C. Kearns, H. Benzian, P. Allison, R.G. Watt, Oral diseases: a global public health challenge, Lancet 394 (10194) (2019) 249–260 (London, England).
[4] D.F. Kinane, P.G. Stathopoulou, P.N. Papapanou, Periodontal diseases, Nat. Rev. Dis. Primers 3 (2017) 17038.
[5] R.G. Caffesse, P.L. Sweeney, B.A. Smith, Scaling and root planing with and without periodontal flap surgery, J. Clin. Periodontol. 13 (3) (1986) 205–210.
[6] R. Singh, S. Sahore, P. Kaur, A. Rani, P. Ray, Penetration barrier contributes to bacterial biofilm-associated resistance against only select antibiotics, and exhibits genus-, strain- and antibiotic-specific differences, Pathog. Dis. 74 (6) (2016) ftw056.
[7] N. Roth, A. Käsbohrer, S. Mayrhofer, U. Zitz, C. Hofacre, K.J. Domig, The application of antibiotics in broiler production and the resulting antibiotic resistance in Escherichia coli: a global overview, Poult. Sci. 98 (4) (2019) 1791–1804.
[8] Y. Chen, Y. Gao, Y. Chen, L. Liu, A. Mo, Q. Peng, Nanomaterials-based photothermal therapy and its potentials in antibacterial treatment, J. Control. Release 328 (2020) 251–262 official journal of the Controlled Release Society.
[9] T. Ding, L. Zhang, J. Han, J. Zhou, Y. Han, Photo-responded antibacterial therapy of reinfection in percutaneous implants by nanostructured bio-heterojunction, Small 19 (7) (2023) e2206265 (Weinheim an der Bergstrasse, Germany).
[10] Y. Li, Z. Miao, Z. Shang, Y. Cai, J. Cheng, X. Xu, A visible- and NIR-light responsive photothermal therapy agent by chirality-dependent MoO3−x nanoparticles, 30(4) (2020) 1906311.
[11] C. Xu, K. Pu, Second near-infrared photothermal materials for combinational nanotheranostics, Chem. Soc. Rev. 50 (2) (2021) 1111–1137.
[12] J. Shinn, S. Lee, H.K. Lee, J. Ahn, S.A. Lee, S. Lee, Y. Lee, Recent progress in development and applications of second near-infrared (NIR-II) nanoprobes, Arch. Pharmacal Res. 44 (2) (2021) 165–181.
[13] Y. Chen, B. Sun, X. Jiang, Z. Yuan, S. Chen, P. Sun, Q. Fan, W. Huang, Double-acceptor conjugated polymers for NIR-II fluorescence imaging and NIR-II photothermal therapy applications, J. Mater. Chem. B 9 (4) (2021) 1002–1008.
[14] Y. Zhao, Y. Liu, Q. Wang, J. Liu, S. Zhang, T. Zhang, D. Wang, Y. Wang, L. Jin, H. Zhang, Carambola-like Bi(2)Te(3) superstructures with enhanced photoabsorption for highly efficient photothermal therapy in the second near-infrared biowindow, J. Mater. Chem. B 9 (35) (2021) 7271–7277.
[15] Y.J. Lin, I. Khan, S. Saha, C.C. Wu, S.R. Barman, F.C. Kao, Z.H. Lin, Thermocatalytic hydrogen peroxide generation and environmental disinfection by Bi(2)Te(3) nanoplates, Nat. Commun. 12 (1) (2021) 180.
[16] F. Liu, T. He, S. Gong, M. Shen, S. Ma, X. Huang, L. Li, L. Wang, Q. Wu, C. Gong, A tumor pH-responsive autocatalytic nanoreactor as a H(2)O(2) and O(2) self-supplying depot for enhanced ROS-based chemo/photodynamic therapy, Acta Biomater. 154 (2022) 510–522.
[17] M. Wang, S. Maragani, L. Huang, S. Jeon, T. Canteenwala, M.R. Hamblin, L.Y. Chiang, Synthesis of decacationic [60]fullerene decaiodides giving photoinduced production of superoxide radicals and effective PDT-mediation on antimicrobial photoinactivation, Eur. J. Med. Chem. 63 (2013) 170–184.
[18] P.L. Lam, R.S. Wong, K.H. Lam, L.K. Hung, M.M. Wong, L.H. Yung, Y.W. Ho, W.Y. Wong, D.K. Hau, R. Gambari, C.H. Chui, The role of reactive oxygen species in the biological activity of antimicrobial agents: an updated mini review, Chem. Biol. Interact. 320 (2020) 109023.
[19] S. Gligorovski, R. Strekowski, S. Barbati, D. Vione, Environmental implications of hydroxyl radicals (•OH), Chem. Rev. 115 (24) (2015) 13051–13092.
[20] J. Cadet, K.J.A. Davies, M.H. Medeiros, P. Di Mascio, J.R. Wagner, Formation and repair of oxidatively generated damage in cellular DNA, Free Radic. Biol. Med. 107 (2017) 13–34.
[21] H. Choi, D.G. Lee, Antimicrobial peptide pleurocidin synergizes with antibiotics through hydroxyl radical formation and membrane damage, and exerts antibiofilm activity, Biochim. Biophys. Gen. Sub. 1820 (12) (2012) 1831–1838.
[22] Y. Liu, Z. Guo, F. Li, Y. Xiao, Y. Zhang, T. Bu, P. Jia, T. Zhe, L. Wang, Multifunctional magnetic copper ferrite nanoparticles as fenton-like reaction and near-infrared photothermal agents for synergetic antibacterial therapy, ACS Appl. Mater. Interfaces 11 (35) (2019) 31649–31660.
[23] Z. Tang, H. Zhang, Y. Liu, D. Ni, H. Zhang, J. Zhang, Z. Yao, M. He, J. Shi, W. Bu, Antiferromagnetic pyrite as the tumor microenvironment-mediated nanoplatform for self-enhanced tumor imaging and therapy, Adv. Mater. 29 (47) (2017) 1701683 (Deerfield Beach, Fla.).
[24] G. Li, K. Lv, Q. Cheng, H. Xing, W. Xue, W. Zhang, Q. Lin, D. Ma, Enhanced bacterial-infected wound healing by nitric oxide-releasing topological supramolecular nanocarriers with self-optimized cooperative multi-point anchoring, Adv. Sci. (2023) e2206959 (Weinheim, Baden-Wurttemberg, Germany).
[25] Z. Yuan, C. Lin, Y. He, B. Tao, M. Chen, J. Zhang, P. Liu, K. Cai, Near-infrared light-triggered nitric-oxide-enhanced photodynamic therapy and low-temperature photothermal therapy for biofilm elimination, ACS Nano 14 (3) (2020) 3546–3562.
[26] D. Fernandes, R.S. Khambata, G. Massimo, E. Ruivo, L.C. Gee, J. Foster, A. Goddard, M. Curtis, M.R. Barnes, W.G. Wade, T. Godec, M. Orlandi, F. D'Aiuto, A. Ahluwalia, Local delivery of nitric oxide prevents endothelial dysfunction in periodontitis, Pharmacol. Res. 188 (2023) 106616.
[27] M. Kielbik, M. Klink, M. Brzezinska, I. Szulc, Z. Sulowska, Nitric oxide donors: spermine/NO and diethylenetriamine/NO induce ovarian cancer cell death and affect STAT3 and AKT signaling proteins, Nitric Oxide 35 (2013) 93–109.
[28] K. Zhang, H. Xu, X. Jia, Y. Chen, M. Ma, L. Sun, H. Chen, Ultrasound-triggered nitric oxide release platform based on energy transformation for targeted inhibition of pancreatic tumor, ACS Nano 10 (12) (2016) 10816–10828.
[29] J. Gehring, B. Trepka, N. Klinkenberg, H. Bronner, D. Schleheck, S. Polarz, Sunlight-triggered nanoparticle synergy: teamwork of reactive oxygen species and nitric oxide released from mesoporous organosilica with advanced antibacterial activity, J. Am. Chem. Soc. 138 (9) (2016) 3076–3084.
[30] P.G. Wang, M. Xian, X. Tang, X. Wu, Z. Wen, T. Cai, A.J. Janczuk, Nitric oxide donors: chemical activities and biological applications, Chem. Rev. 102 (4) (2002) 1091–1134.
[31] M. Wan, H. Chen, Q. Wang, Q. Niu, P. Xu, Y. Yu, T. Zhu, C. Mao, J. Shen, Bio-inspired nitric-oxide-driven nanomotor, Nat. Commun. 10 (1) (2019) 966.
[32] J. Yu, R. Zhang, B. Chen, X. Liu, Q. Jia, X. Wang, Z. Yang, P. Ning, Z. Wang, Y. Yang, Injectable reactive oxygen species-responsive hydrogel dressing with sustained nitric oxide release for bacterial ablation and wound healing, 32(33) (2022) 2202857.
[33] X. Fang, S. Cai, M. Wang, Z. Chen, C. Lu, H. Yang, Photogenerated holes mediated nitric oxide production for hypoxic tumor treatment, 60(13) (2021) 7046-7050.
[34] A. Gupta, R. Das, G. Yesilbag Tonga, T. Mizuhara, V.M. Rotello, Charge-switchable nanozymes for bioorthogonal imaging of biofilm-associated infections, ACS Nano 12 (1) (2018) 89–94.
[35] O. Ivanov, M. Yaprintsev, R. Lyubushkin, O. Soklakova, Enhancement of thermoelectric efficiency in Bi2Te3 via rare earth element doping, Scr. Mater. 146 (2018) 91–94.
[36] H. Qin, L. Xie, Z. Zhang, D. Qin, F. Guo, W. Cai, Q. Zhang, J. Sui, Rare earth ytterbium enhanced thermoelectric properties of p-type Bi0.5Sb1.5Te3, 114(12) (2019) 123901.
[37] Y. Xi, Y. Wang, J. Gao, Y. Xiao, J. Du, Dual corona vesicles with intrinsic antibacterial and enhanced antibiotic delivery capabilities for effective treatment of biofilm-induced periodontitis, ACS Nano 13 (12) (2019) 13645–13657.
[38] Y. Zhang, D. Li, J. Tan, Z. Chang, X. Liu, W. Ma, Y. Xu, Near-infrared regulated nanozymatic/photothermal/photodynamic triple-therapy for combating multidrug-resistant bacterial infections via oxygen-vacancy molybdenum trioxide nanodots, Small 17 (1) (2021) e2005739 (Weinheim an der Bergstrasse, Germany).
[39] M.A. De Groote, F.C. Fang, NO inhibitions: antimicrobial properties of nitric oxide, Clin. Infect. Dis. 21 (Suppl 2) (1995) S162–S165 an official publication of the Infectious Diseases Society of America.
[40] Q. Gao, X. Zhang, W. Yin, D. Ma, C. Xie, L. Zheng, X. Dong, L. Mei, J. Yu, C. Wang, Z. Gu, Y. Zhao, Functionalized MoS2 nanovehicle with near-infrared laser-mediated nitric oxide release and photothermal activities for advanced bacteria-infected wound therapy, 14(45) (2018) 1802290.
[41] W. Wang, X. Cheng, J. Liao, Z. Lin, L. Chen, D. Liu, T. Zhang, L. Li, Y. Lu, H. Xia, Synergistic photothermal and photodynamic therapy for effective implant-related bacterial infection elimination and biofilm disruption using Cu(9)S(8) nanoparticles, ACS Biomater. Sci. Eng. 5 (11) (2019) 6243–6253.
[42] Y. Wang, S. Li, X. Xing, F. Huang, Y. Shen, A. Xie, X. Wang, J. Zhang, Self-assembled 3D flowerlike hierarchical Fe_3O_4@Bi_2O_3 Core–shell architectures and their enhanced photocatalytic activity under visible light, Chem. Eur. J. 17 (17) (2011) 4802–4808.
[43] M. Tong, F. Liu, Q. Dong, Z. Ma, W. Liu, Magnetic Fe3O4-deposited flower-like MoS2 nanocomposites for the Fenton-like Escherichia coli disinfection and diclofenac degradation, J. Hazard. Mater. 385 (2020) 121604.
[44] M. Bhagavantha Reddy, V.N. Mulay, V. Devender Reddy, P. Venugopal Reddy, Charge transport in mixed Li Ti ferrites, Mater. Sci. Eng. B 14 (1) (1992) 63–69.

[45] Q. Chen, X. Shan, S. Shi, C. Jiang, T. Li, S. Wei, X. Zhang, G. Sun, J. Liu, Tumor microenvironment-responsive polydopamine-based core/shell nanoplatform for synergetic theranostics, J. Mater. Chem. B 8 (18) (2020) 4056–4066.
[46] Z. Liu, X. Zhao, B. Yu, N. Zhao, C. Zhang, F.J. Xu, Rough carbon-iron oxide nanohybrids for near-infrared-II light-responsive synergistic antibacterial therapy, ACS Nano 15 (4) (2021) 7482–7490.
[47] J.R. Lancaster, A tutorial on the diffusibility and reactivity of free nitric oxide, Nitric Oxide 1 (1) (1997) 18–30.
[48] J. Huang, J. Zhou, J. Zhuang, H. Gao, D. Huang, L. Wang, W. Wu, Q. Li, D.P. Yang, M.Y. Han, Strong near-infrared absorbing and biocompatible CuS nanoparticles for rapid and efficient photothermal ablation of gram-positive and -negative bacteria, ACS Appl. Mater. Interfaces 9 (42) (2017) 36606–36614.
[49] C.I. Kothe, J.P. Pessoa, P.S. Malheiros, E.C. Tondo, Assessing the growth of Staphylococcus aureus and Escherichia coli on fruits and vegetables, J. Infect. Dev. Ctries. 13 (6) (2019) 480–486.
[50] K. Schilcher, A.R. Horswill, Staphylococcal biofilm development: structure, regulation, and treatment strategies, Microbiol. Mol. Biol. Rev. 84 (3) (2020) e00026–19.
[51] J. Zhang, Y. Feng, J. Mi, Y. Shen, Z. Tu, L. Liu, Photothermal lysis of pathogenic bacteria by platinum nanodots decorated gold nanorods under near infrared irradiation, J. Hazard. Mater. 342 (2018) 121–130.